Innovative Direct Solar Receiver-Storage Systems for Heat Production (Inno-DSS)

TKI Urban Energy project 'Inno-dss'. Project number: 1621202
Datum: 26-1-2022
Authors: Amir Mahmoudi, Mohammad Mehrali, Gholamabbas Sadeghi, Chung-Yu Yeh

Contents

Chapter 1. Introduction 3

Chapter 2. Development of shape-stabilized PCM 4

2.1. Materials 5

2.2. Functionalization of the GNPs 5

2.3. Preparation of the SAT-SPM-GNPs (SSG) composite PCMs 5

2.4. Characterization 6

2.5. Results and discussion 7

2.5.1. Effect of SPM mass fraction on nucleation of SAT 7

2.5.2. Phase change and supercooling behaviors of SAT-SPM 7

2.5.3. Crystallinity and chemical compatibility of SAT-SPM salt system 9

2.5.4. Shape Stabilized PCMs (SSPCMs) 11

2.5.6. Phase change and supercooling behaviors of SSPCMs 12

2.5.7. Thermal and shape stability of SSPCMs 13

2.5.8. Solar-thermal conversion and storage performance of SSPCMs 14

2.5.9. Thermal conductivity and reliability of SSPCMs 18

Chapter 3. Simulation of solar collector with phase change materials 19

3.1. Collector design 19

3.2. Collector geometry 19

3.3. Discharging and charging scenarios 20

3.4. Discharging scenario 21

3.5. Charging scenario 21

3.6. Design indicators for discharging scenario 22

3.7. Discharging scenario 22

Chapter 4. Construction and test of solar collector 26

4.1. Direct-absorption parabolic trough solar collector 26

4.1.1. Implementation of experiments for the PTC 28

4.1.2. Results 29

4.2. Implementation of the experiment for cylindrical solar collector 31

4.2.1. Results 31

5. Direction of future work 32

References: 33

Chapter 1. Introduction

In Europe, more than 50% of the energy used in households is in the form of heat [1], and supplying domestic hot water is still the major application of solar thermal system. However, the weather-dependent and intermittent characteristics of solar irradiance hinder the solar energy exploration. One of the most promising way to tackle this problem is using heat storage together with solar thermal collectors. In this way the thermal storage unit stores the excess energy generated during the day and releases it when it is needed (i.e., during the night).

The sensible and latent heat storage are most common thermal energy storage techniques in cooperation with solar thermal collectors. Sensible heat storage is most widely used for daily and short-term thermal energy storage due to its technology maturity and low cost, e.g., hot water tanks. However, it cannot store heat for a longer period mainly due to the large heat loss. Moreover, large storage volumes are required because of the water's low volumetric energy density. On the contrary, latent heat storage (i.e., phase changer materials) offers higher energy density and smaller temperature variation during phase transition which allows storing larger quantity of heat in smaller volume and supply the heat with less heat loss [2, 3].

A high heat capacity and suitable melting temperature are the crucial factors in selection of phase change materials (PCMs) for the heat storage applications. One of the candidates that fits the domestic application is sodium acetate trihydrate (SAT). SAT is an inorganic PCM which has a higher latent heat storage capacity compared to organic PCMs. The melting point of SAT is around 58 °C [4] that matches the domestic hot water temperature which is ranged from 40 °C to 60 °C. SAT is also a cheap and a safe material but does suffer from problems like supercooling, phase segregation [5, 6], and phase change stability. Furthermore, in the literature it is found that the thermal conductivity of SAT is low, ranging from 0.17 to 0.7 W/mK [7]. The leakage issue of PCMs in their liquid phase also causes high operation and maintenance cost. These problems hinder the SAT from becoming a suitable PCM. To solve the issues of SAT has, a new type of PCM has been developed (i.e., shape-stabilized PCM (ssPCMs)).

ssPCMs is one of the heat transfer enhancement methods on PCM by impregnating the PCM into the supportive materials [8, 9]. These supportive materials have to be porous like expanded graphite (EG), carbon nanotubes, metal foam, and expanded perlite [10], since their high absorption surface can prevent leakage, and thus makes the PCM shape stabilized. Xiao et al. [11] impregnated EG with SAT, and added Na_2HPO_4 as a nucleating agent to prevent

supercooling. CuS was added to improve the light to thermal conversion. Li et al. [12] experimentally tested the performance of ssPCMs in the real field. The EG was added into the erythritol as composite PCM for the mid-temperature range of 120 °C. An excavated tube of solar collector was used. Furthermore, a pump was attached and water was used as heat transfer fluid (HTF). The collector was placed outside and heated by the sun. In this study the solar irradiance during the day has been recorded and at the end of the day, the discharging process began.

The design of the PCM energy storage systems have to consider the characteristics of PCM and its application field. Nkwetta et al. [13] reviewed the existing approach to the PCM storage system that integrated the hot water tanks and the solar collectors for the domestic application. The natural barrier of low thermal conductivity in PCM and the influence of HTF using water and air were discussed. Zhangyuan et al. [14] overviewed the PCM applications on the solar water heating system. The system configuration with solar collector and the weather condition included analysis were discussed. It pointed out the selection of material influences the solar energy collection efficiency. The optimized operation temperature and the size of storage were changed with the type of material selected.

The literature presented shows that the feasibility of ssPCMs applied in absorbing solar irradiance and storing the thermal energy. To further improve this concept, in this study, an inorganic ssPCMs, i.e., SAT-SPM-EG (SSE) for direct solar absorption will be investigated. Moreover, a simulation process has been conducted by COMSOL software for optimizing the dimensions of the equipment before their construction and implementation.

Chapter 2. Development of shape-stabilized PCM

The intermittent nature of solar radiation for solar driven applications providing the vast opportunity for phase change materials(PCMs) to reduce the gap between supply and demand of energy. Nevertheless, the widespread utilization of PCMs is limited due to the flow of liquid PCMs during melting, phase separation, supercooling and low heat transfer rate. The ongoing progression of research in this field reveals that there is a high demand for shape stabilized PCMs (SSPCMs) with high energy storage capacity and fast charging and discharging rates.

Here, we demonstrated the facile route to synthesize novel salt hydrate based SSPCMs via incorporation of the functionalized graphene nanoplatelets (GNPs).

2.1. Materials

Sodium acetate trihydrate; 99% (SAT,$C_2H_9NaO_5$) was purchased from VWR Chemicals, Germany. Sodium dihydrogen phosphate monohydrate (SPM, $Na_2HPO_4.H_2O$) served as nucleating agent was provided by Sigma Aldrich,Germany. Graphene nanoplatelets (GNPs,GRADE C) with different specific surface areas (300, 500 and 750 m^2/g) were obtained commercially from XG science, USA. For the functionalization of the GNPs, 1-pyrenecarboxylic; 98% ($C_{17}H_{10}O_2$) was purchased from Sigma Aldrich, Germany.

2.2. Functionalization of the GNPs

Prior to experiments, GNPs with different specific surface areas were dried in an oven at 80 °C for 24 h to remove free water on the surface. Noncovalent functionalized GNPs were obtained by sonicating GNPs (10 g) and 1-pyrenecarboxylic acid (1 g) in ethanolic solution for 2 h, followed by overnight stirring at room temperature and washing process. The dried Hp-GNPs were collected after overnight drying in vacuum.

2.3. Preparation of the SAT-SPM-GNPs (SSG) composite PCMs

In the current study, the SSG form stable composite PCMs were prepared by a physical blending method using SAT-SPM eutectic mixture as PCM and Hp-GNPs with various specific surface areas as matrix material, solar absorber and thermal conductivity enhancer. At first, SAT-SPM mixtures with varying mass ratio of SPM were obtained by adding corresponding amounts of nucleating agent (0.5, 1, 2 and 3 wt%) into the pure salt hydrate. They were mixed in a sealed glass flask and heated to 75 °C until complete melting and stirred for 1 h to obtain the clear SAT-SPM mixture. The mixture was cooled down and then mortar and pestle were used to grind samples by hand to provide SAT-SPM fine powder. The SSG composite PCMs were prepared via a solution impregnation method for Hp-GNPs with different specific surface areas (300, 500, 750 m2/g) as shown in Fig. 1. Subsequently, the SAT-SPM powder with proper composition was added into a certain amount of Hp-GNPs (5 wt%). Then the resulting mixture was manually mixed and grinded following stirring for 1 h at 75 °C. Finally, the resulting mixtures were cooled down and solidified at room temperature to obtain SSG composite PCMs. The optimal mass fraction of GNPs to achieve form stable PCMs were determined by preparing the SSG pellets and letting the excess SAT to be absorbed by filter paper at 75 °C in closed glass jar.

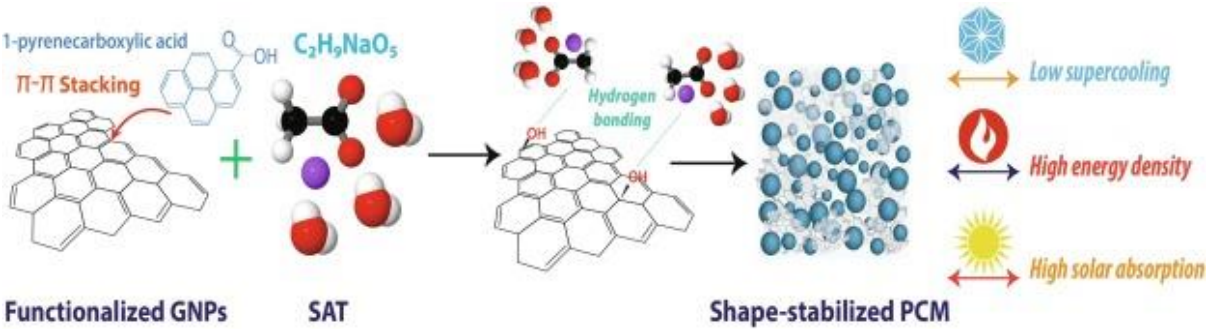

Fig. 1. Schematic illustration of shape stabilized PCM synthesis.

2.4. Characterization

The JEOL (JSM-6010LA) scanning electron microscope was used for SEM imaging. The transmittance, absorption and reflectance spectra of the SSPCMs were measured using a UV–vis-NIR (PerkinElmer, Lambda950) spectrophotometer with wavelength accuracy of ±0.1 nm. The crystallography analysis was investigated using the Bruker D2 Phaser desktop X-ray diffractometer with a Cu source for 2θ = 5 to 40 °. The crystal morphology of the pure SAT and obtained SSPCMs were observed using a polarized optical microscope (POM, Axioskop 40POL, Germany) equipped with a high-resolution CCD camera. The phase change temperatures and enthalpy of fusion during the charging and discharging process for composite PCMs were obtained by differential scanning calorimeter (NETZSCH DSC 214 Polyma-Error ±0.05% to ±0.2%) at a heating rate of 2 °C/min. The weight loss and thermal stability of PCMs are examined by thermogravimetric analysis (TA instruments TGA 550-Error 0.01%) for a temperature range of 50 to 400 °C and heating rate of 10 °C/min in purified nitrogen atmosphere. The Fourier-transform infrared spectroscopy was used to analyze the chemical composition of the samples in the wavenumber range of 4000–400 cm^{-1}on a PerkinElmer ATR (Spectrum 100). Thermal conductivity of samples was measured by transient hot wire method using KD2 Pro thermal properties analyzer (Decagon Devices,USA) with a SH-1 probe. Prior to the measurement, the samples were compressed into cylindrical block with size of 25.4 mm × 30 mm using a home-made mold. Then, the blocks were located in 3D printed sample holder and temperature was controlled during the experiment using programmable thermal bath (Julabo-DYNEO 900F). The accuracy and the reproductivity for the measurement were within ±5% and ±2%, respectively. The accelerated thermal cycling test was performed to evaluate the thermal reliability of the prepared SSPCMs after 500 cycles. Thermal cycling

test was performed for the temperature range of 30–75 °C and DSC analysis provided the enthalpy changes as well as heating and cooling curves after experiencing 100 and 500 cycles.

The light-to-thermal conversion performance was evaluated using a Sol3A Class AAA Solar Simulator(94023A, Newport, USA) with a 450 Watt Xenon lamp source and high flux beam concentrator that illuminated the (15 mm) diameter spot. The samples were placed in a thermal insulation sample holder where a quartz window covered the top of the cylinder and they were directly illuminated by a simulated sunlight source (≃700 mW/cm^2). The temperature variations were also recorded using the a data logging unit (Omega-TC08).

2.5. Results and discussion

2.5.1. Effect of SPM mass fraction on nucleation of SAT

To investigate the effect of sodium dihydrogen phosphate monohydrateand (SPM) on the nucleation behavior and thermal characteristics of the sodium acetate trihydrate (SAT) composite. salt system, in depth analyses were carried out with varying content (0.5, 1, 2, 3 wt%) of SPM. SAT consistently shows intrinsic high supercooling degree (ΔT) deteriorating the thermal reliability and heat storage capability. It was found from previous studies that pure molten SAT could be supercooled below 0 °C offering the maximum ΔT of about 80 °C. In this study, SPM was selected as nucleating agent for efficacious supercooling elimination due to its excitation as hydrate structure similar to SAT at temperatures under the melting point of SPM (≃120 °C). The SPM solubility in molten SAT and its mass fraction play key roles in the acceleration of the crystallization rate within SAT-SPM salt mixtures. The low solubility of the SPM in molten SAT while having a hydrated structure provides a huge advantage over other nucleating agents such as disodium hydrogen phosphate (DSP), tetrasodium pyrophosphate decahydrate (TPD), anhydrous sodium acetate (SAA), sodium tetraborate decahydrate (STD) and sodium metasilicate nonahydrate (SMN).

2.5.2. Phase change and supercooling behaviors of SAT-SPM

A daring goal is to provide low supercooling degree without extensive effects on the melting point and latent heat of SAT. The DSC curves of SAT-SPM with different SPM mass fractions are illustrated in Fig. 2 and in detail results were tabulated in Table 2. The DSC curves for SAT-SPM mixtures reveal a single peak, indicating the eutectic mixture of SAT and SPM. The DSC measurements were performed with low heating and cooling rate of 2 °C/min to suppress

the effect of phase separation. Fig. 2 (b-e) shows the melting and solidification curves of SAT containing different mass ratios of SPM. As shown in Table 2, the onset temperatures of melting (T_m) for SAT-SPM eutectic mixtures were decreased with the mass fraction increment of SPM. The phenomenon can be explained considering the interaction force debilitation of sodium acetate with H_2O molecules caused by Na^+ions in SPM. When the mass fraction of SPM was higher than 1 wt%, the melting temperatures of the eutectic salt mixtures approached 54 °C and remained comparatively constant with a further SPM mass fraction increment. DSC measurements of two full cycles of melting and solidification were performed for better understanding of the phase change process in SAT and SAT-SPM mixtures. A significant enthalpy change was observed between the first and second melting cycles that can be attributed to the quality of thermal contact between the samples and aluminum pans or, to phase separation effects. The second cycle melting enthalpy value is in good agreement with reported values for pure SAT (≃270 J/g). Building on these results, the supercooling degree of SAT-SPM mixtures with different SPM contents (0.5, 1, 2, 3 wt%) were 2.3, 0.2, 0.3, 0.7 °C, respectively (see Fig. 2 (f) for details).From these results, it is evident that addition of SPM almost demolished the supercooling effect in SAT and reduced it by up to 0.2 °C. By taking into account phase change temperatures and supercooling degrees, the optimum concentration of SAT-SPM was estimated to be about 1wt% in SAT-SPM eutectic salt system. More importantly, the SAT-SPM-1wt% mixture represented a high latent heat of fusion (267.2 J/g) which was about 99 wt% of that of pure SAT (269.3 J/g).

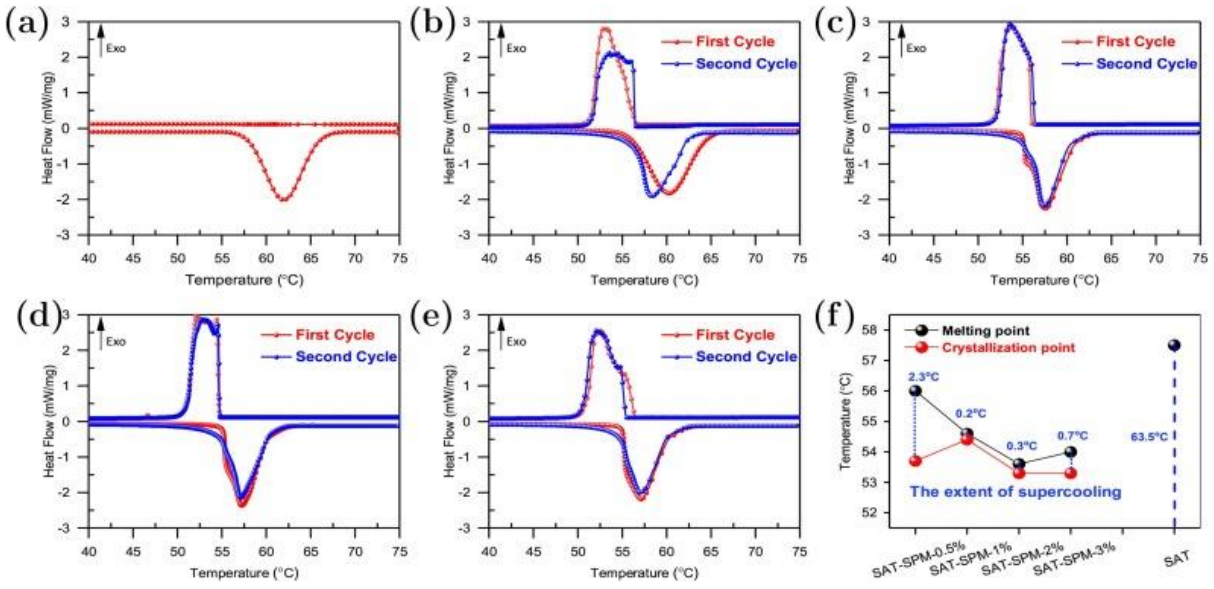

Fig. 2. DSC melting and solidification curves of (a) Pure SAT; (b) SAT-SPM-0.5 wt%; (c) SAT-SPM-1 wt%; (d) SAT-SPM-2 wt%; (e) SAT-SPM-3 wt%; (f) The extent of supercooling for different SPM content.

Table 2. DSC results for SAT-SPM composite PCMs with different SPM mass fraction.

	Melting process				**Crystallization process**				
Sample	Tm1 **(°C)**	**ΔH_1(J/g)**	Tm2**(°C)**	**ΔH_2(J/g)**	Ts1 **(°C)**	**ΔH_1(J/g)**	Ts2 **(°C)**	**ΔH_2(J/g)**	**Supercooling degree (°C)**
SAT	58.1	298.6	58.2	269.3	−11.3	240.5	−5.3	230.2	63.5
SAT-SPM-0.5 wt%	56.9	297.1	56.5	256.1	54.7	251.7	54.2	249.6	2.3
SAT-SPM-1 wt%	55.8	292.3	55.1	267.2	54.9	261.3	54.9	260	0.2
SAT-SPM-2 wt%	55.7	290.3	54.1	261.8	53.9	261.2	53.8	260.6	0.3
SAT-SPM-3 wt%	55.6	288.4	54.5	261.6	54.35	262.1	53.8	259.5	0.7

T_m and Ts: Melting and solidification onset temperatures for the first and second cycles ΔH: Enthalpy on DSC curve Supercooling degree = Tm2 (melting) -Ts2 (Crystallization)

2.5.3. Crystallinity and chemical compatibility of SAT-SPM salt system

The crystalline structures of SAT powder, supercooled SAT, SPM powder and SAT-SPM mixtures were analyzed by XRD and the resulting diffraction patterns are illustrated in Fig. 3 (a). The XRD pattern for SAT powder shows a sharp diffraction peak at 11.7° assigned to the feature peak (110) of SAT. The strong peaks at 16.9°, 22.5° and 29.7° attributed to the feature peaks (020), (221) and (402) of SAT, respectively. All diffraction peaks of the sample can be well indexed to the phase of SAT (JCPDS No. 29–1160). It confirms that SAT has mono-clinic crystal system in which the Na^+ion has distorted octahedral coordination with six oxygen atoms [41].

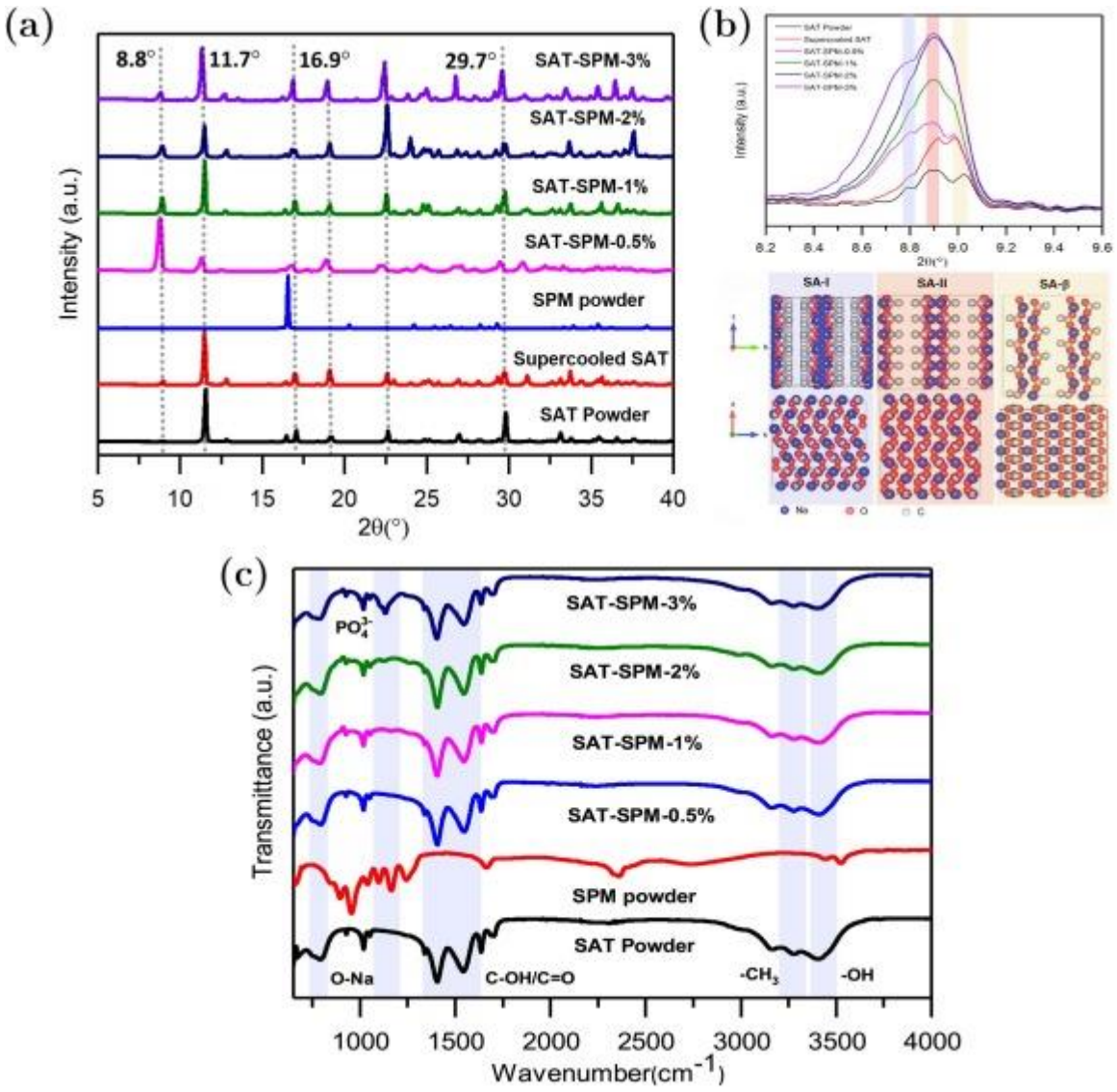

Fig. 3. (a) XRD patterns (b) Zoomed part of XRD pattern for crystallization products of SA and (c) FTIR spectra of SAT, SPM powders and SAT-SPM with different mass fraction of SPMs.

A new diffraction peak was observed for supercooled SAT at 8.8° due to the formation of sodium acetate (SA,CH_3COONa) molecules that is in good agreement with the orthorhombic crystal system of SA (JCPDS No. 29–1158). The presence or absence of hydrogen bonds within the SA and SAT crystals causes the largest crystal structure difference. Anhydrous sodium acetate has three crystal structures named as SA-I, SA-II, and SA-β which of the crystal structures are demonstrated in Fig. 3 (b). The zoomed XRD patterns from $2\theta = 8.2$ to 9.4° in Fig. 3 (b) represent the characteristic peak consistent with the (010) plane. Three asymmetric peak shapes are observed for SAT-powder, supercooled SAT and SAT-SPM-0.5% at $2\theta = 8.78$, 8.85, and 8.95° advocating that all three crystal structures of SA crystallized concomitantly to form the CH_3COONa crystals within their solid structure. It can be seen that

addition of SPM has an effect on crystallization products as only one diffraction peak for SA-II at 8.85° can be indicated for SAT-SPM-1% and SAT-SPM-2% while addition of more SPM changes products to SA-I and SA-II. The previous studies on crystal structure of SA suggested the stable form of the crystal for SA-II. It is anticipated that formation of stable SA crystals leads to strong nucleation sites to achieve homogeneous nucleation. The initial liquid state such as temperature has shown considerable effect on kinetics of SAT crystallization. Moreover, a stronger SA diffraction peak at 8.85° compared with SAT peak at 11.7° is observed in the XRD pattern of the SAT-SPM-0.5% which can be evidence of the phase separation phenomenon. The SPM powder has very strong diffraction peak at 16.4° attributed to the (011) peak and that can be well indexed to the Orthorhombic phase of SPM (JCPDS No. 11–0651). Due to the low mass fraction of SPM, the SPM diffraction peaks are not recognizable in XRD patterns of SAT-SPM salt mixtures. The results from DSC measurement likely corroborate the XRD data by showing lower supercooling degree for SAT-SPM-1%.

The ATR spectra of SAT, SPM and SAT-SPM eutectic mixtures at room temperature are shown in Fig. 3 (c). For SAT powder, major peaks at 1350 and 1559 cm^{-1} are caused by the C-OH and -C=O stretching vibrations affected by vibration coupling. The peaks at 3480 and 3280 cm^{-1} can be assigned to stretching vibration of O-H group. The peak at 780 cm^{-1} corresponds to the deformation vibration of O-Na and the -CH_3 stretching vibration can be detected at 2916 cm^{-1}. These characteristics were also observed for the SAT-SPM mixtures. Meanwhile, the SPM showed a major characteristic peak of PO43- at 1100 cm^{-1} that can be detected only at higher concentration of SPM. FTIR analysis is also in good agreement with XRD results indicating the physically fabricated SAT-SPM salt system without any changes in their chemical properties.

2.5.4. Shape Stabilized PCMs (SSPCMs)

Real-world applications of salt hydrate based composite PCMs for solar energy capture and storage requires a low degree of supercooling, high thermal conductivity and energy density, absence of phase separation, great photo-thermal conversion capability that need to be taken into consideration. An elegant forerunner towards these characteristics is proposed in this study by utilizing modified GNPs as a host matrix. The interesting properties of GNPs such as high thermal conductivity and specific surface area make them good candidates as host matrices for SAT-SPM salt systems. In this study three types of GNPs with different specific surface areas of 300, 500 and 750 m^2/g were considered to prepare shape stabilized SAT-SPM/GNP (SSG) composites. Previous studies have shown that the hydrophilic nature and good wettability

properties of the host material can provide a great platform for crystal formation and suppress the supercooling and phase separation effects[45]. The hydrophilic GNPs were prepared by noncovalent functionalization of GNPs with 1-pyrenecarboxylic acid based on a previously reported method[46]. The functionalization of carboxylic acid groups(-COOH) as hydrophilic functional groups on the surface of GNP nanosheets was achieved via a nondestructive - stacking mechanism (aromatic interaction) as shown in Fig. 1. These functional groups do not dimerise in SAT-SPM, but form hydrogen bonds with water molecules of SAT-SPM and greatly restrict the water molecular movement providing a barrier against phase separation and fluidity of melted SAT-SPM.

2.5.6. Phase change and supercooling behaviors of SSPCMs

The DSC curves of SAT-SPM-1% and SSG composite PCMs during three cycles of the melting and crystallization processes are separately shown in Fig. 4 (a-c) and in details phase change parameters are listed in Table 3. Notably, the distinct difference between ΔH_m and ΔH_S that was observed most likely caused by the partial dehydration of the salt during the heating process. The SSG composite PCMs showed similar single peak as the SAT-SPM salt mixture. However,the phase change peaks became broader by addition of GNP nanosheets without considerable changes of melting and solidification onset temperatures (T_m & T_s) which can be explained by the size distribution of the crystallites. It is anticipated that the GNP nanosheets will disturb the hydrogen bonds within the salt structure building up needle-like crystals that spread radially within SSG composites during crystal growth. Intimately linked, the crystal size will effect the melting and solidification temperature ranges. Moreover, SSG composite PCMs containing hydrophilic GNPs provided almost similar supercooling degree values compared with SAT-SPM. The hydrophilic surface of Hp-GNPs including carboxyl(COOH) groups provided the immense compatibility and wettability with the SAT-SPM mixture that boosted the attachment and offered heterogeneous nucleation for crystal growth of salt mixture on its surface. Advantageously, the strong interaction of carboxyl group with Na^+,CH_3COO^- and H_2O molecules offers an intensive adherence between the ions and the crystals repressing the phase separation.

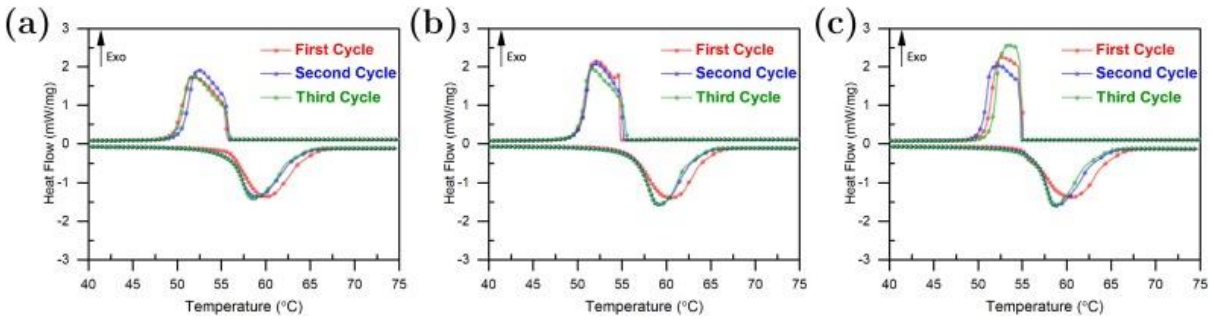

Fig. 4. DSC melting and solidification curves of (a) SSG300; (b) SSG500; (c) SSG750.

Table 3. DSC results for SSG composite PCMs with different specific surface area of Hp-GNPs.

	Melting process		**Crystallization process**				
Sample	**T_m (°C)**	**ΔH_m(J/g)**	**T_s (°C)**	**ΔH_s (J/g)**	ηimp(%)	Rimp(%)	**Supercooling degree (°C)**
SAT-SPM-1%	55.1	267.2	54.9	260	100	100	0.2
SSG300	54.9	230.8	54.6	220.7	85.6	86.4	0.3
SSG500	55.2	238.2	55	230.1	88.8	89.1	0.2
SSG750	55.1	248.3	55	245.2	93.6	92.9	0.1

2.5.7. Thermal and shape stability of SSPCMs

Shape stability is crucial to maintain a high energy density by hindering the leakage of molten PCM during the phase change process. Advantageously, the form stable structure provides consistent heat transfer properties along with the decrement of volume thermal expansion. To further investigate the shape stability of SSG composites, a leakage test was carried out visually as exemplified in Fig. 5(a-c). The powder samples were poured into glass containers and re-melted at 75 °C. Then, the glass containers were placed upside down as shown in Fig. 5b and subjected to a temperature of 75 °C for one hour. The SAT-SPM sample completely melted and leaked out while the SSG composites showed small traces of black particles that were not attached properly during the melting process. It is evident that Hp-GNPs provides a proper surface functionality and physical interaction to maintain shape stability during the phase transition process. Thermal stability of SAT, SAT-SPM and SSG composites were evaluated by means of TGA analysis and the results are illustrated in Fig. 5d. SAT has three water molecules in its structure (≃40% of the SAT molecular weight) that have completely vanished to form Sodium acetate when the sample has been heated up to 155 °C. Sodium acetate was

further degraded at 450 °C into Na_2O. For SAT-SPM and SSG composites, the thermal degradations happened in comparable steps as SAT. Further attention on the first degradation indicates that addition of GNP nanosheets delayed the dehydration process but not to a significant degree.. The weight loss percentage of SAT, SAT-SPM, SSG300, SSG500 and SSG750 for desired working temperatures of 30 to 100 °C were 16%, 13%, 12%, 11% and 9.5% while the maximum loss rate occurred in the range of 70–80 °C. The small thermal stability increment for SSG composite PCMs shows that Hp-GNPs can act as thermal barrier to slow down the evaporation speed and confine the water molecules within the SSG structure by forming hydrogen bonds.

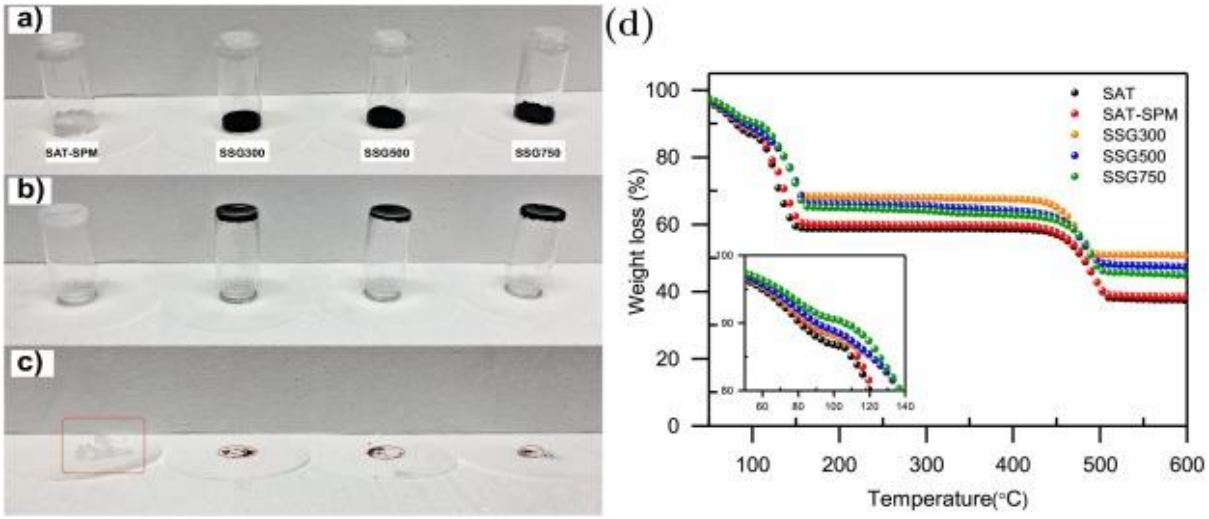

Fig. 5. (a-c) Shape stability performance and (d) TGA thermograms of pure SAT, SAT-SPM and shape stabilized SSG composites.

2.5.8. Solar-thermal conversion and storage performance of SSPCMs

The prime solar energy capturing, storage and heat transfer are the key frameworks to develop highly efficient photo-thermal conversion system. In this approach, solar photons are captured by the SSPCM surface and converted directly to heat raising the temperature of PCM indirectly by heat conduction within the composite structure. The photo-thermal performance of the PCM materials is directly related to their radiation absorption capabilities. Consequently, UV–vis-NIR spectroscopy was executed for precise measurement of transmittance and reflectance spectra to attain the detailed absorbance spectra as shown in Fig. 6. The AM 1.5 global solar spectrum is illustrated in the background of the graphs indicating the solar energy intensity or flux distribution at all wavelengths. Sunlight power is composed (by total energy) of about 5% ultraviolet light(below 400 nm), 42% visible light(400 to 700 nm) and 53% infrared light (above 700 nm) so the visible and NIR radiation accounts for 95% of solar energy that is of

great importance for solar-thermal applications.The transmittance spectra in Fig. 9a represent zero transmittance for SSG composites at all wavelengths while SAT and SAT-SPM samples transmitted some portion of the light. Interestingly, the reflectance spectra in Fig. 9b stipulates that SAT and SAT-SPM samples reflect some portion of NIR as well as 88 and 73% of the visible light,respectively.However, the SSG composites exhibited almost linear reflectance spectra data with low reflectance between 8 to 13%. The absorbance spectra confirm the low absorption of SAT and SAT-SPM in the UV and visible range plus some part of NIR region. The absorbance spectra of SSG300, SSG500 and SSG750 revealed the high solar absorbance of 86, 89 and 93% due to the excellent absorptivity of GNPs nanosheets. Among them, the SSG750 with higher specific surface area of GNPs provided better light absorption capacity that understood by the higher number of graphene nanosheets on the absorbing surface.

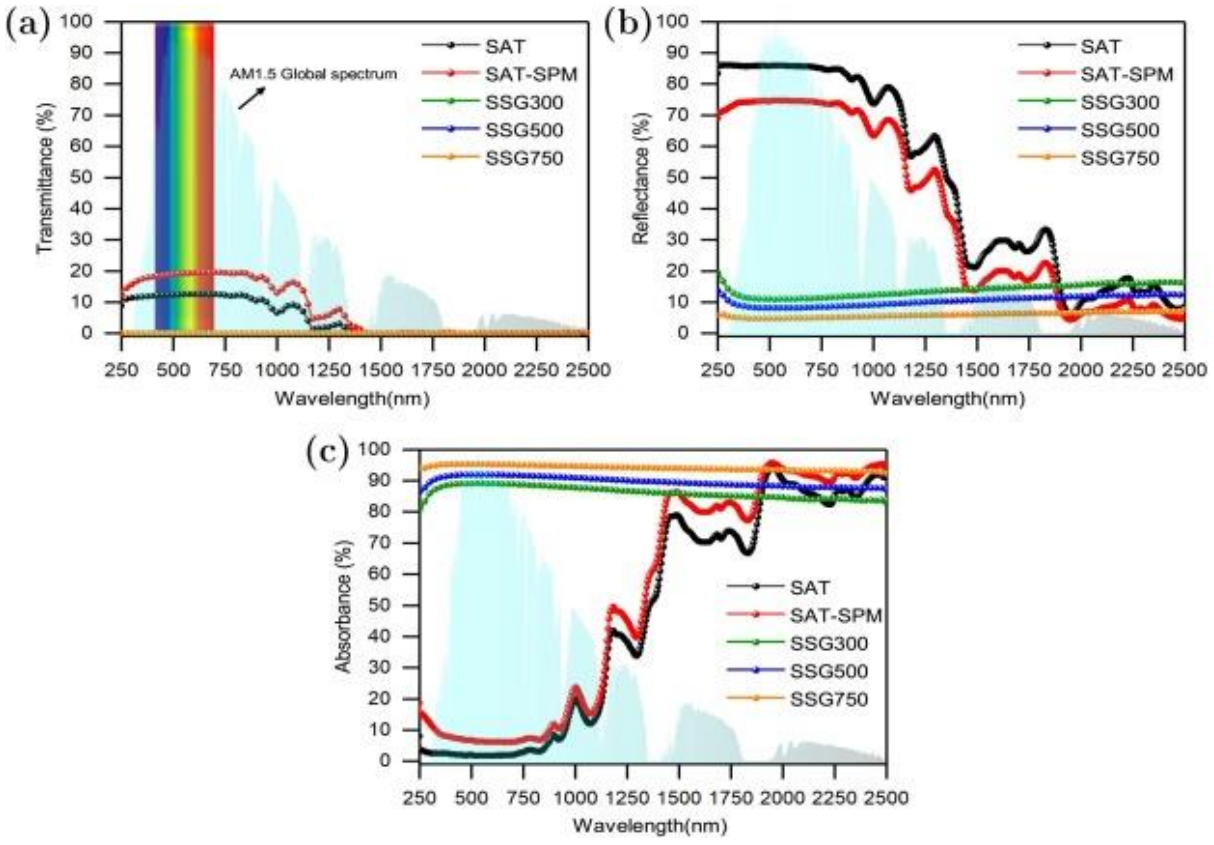

Fig. 6. (a) Optical transmittance (b) reflectance and (c) absorbance spectra of pure SAT, SAT-SPM and shape stabilized SSG composites.

The photo-thermal energy conversion and storage performance of SAT, SAT-SPM and SSG composite PCMs was examined by locating the samples with the same weight and thickness inside the insulated holder with quartz window on top and exposing them to simulated solar illumination (AM 1.5) with a constant intensity of 700 mW/cm^{-2}as shown in Fig. 7a. The

temperature was recorded at the bottom of the sample by locating the thermocouple in the center for charging and discharging steps. Fig. 7(a) shows the graph for SAT indicating the slow temperature rise and gradually reaching the solid–liquid phase change then rising rapidly to the steady-state temperature of about 80 °C which takes about 1620s. Subsequently, by turning off the incident light, the temperature of the SAT decreases rapidly while the energy is discharged by triggering nucleation confirming the supercooling phenomenon. In contrast, the releasing stage of the stored heat for SAT-SPM and SSG composites can be detected without supercooling effects in Fig. 7(c-f). Two charging and discharging cycles with dissimilar final temperature of 80 and 75 °C were performed for SAT-SPM and SSG composites to evaluate the effect of working temperature on their photo-thermal performance and efficiency. Furthermore, as can be seen clearly from the graphs, the SSPCMs showed significant improvement in photo-thermal performance of SAT-SPM salt mixture by reducing the charging time to almost one-third, from 1176s (SAT-SPM) to 424s(SSG300). The photo-thermal performance of SSPCMs was further evaluated by calculating the photo-thermal efficiency based on the temperature graphs and DSC results for the PCMs. The photo-thermal efficiencies at 40, 60 and 70 °C are demonstrated in Fig. 8 (a) for different PCMs. It can be realized that the maximum efficiency was achieved at 60 °C where the phase transition completed due to the rapid increase in heat storage capacity. Consequently, SSG composites have shown considerable high solar-to-thermal energy storage efficiencies of 87.2–92.6% at 60 °C that were decreased to 70.2–73.1% at 70 °C owing to higher thermal losses to their surroundings at higher temperatures. The efficiency calculations from two heating cycles with different final temperatures showed a small variance of less than 5% suggesting the good photo-thermal reliability for prepared SSPCMs. Indisputably, the prepared salt hydrate based SSPCMs simultaneously possess high energy density with an excellent solar thermal efficiency nominating them as very promising materials for solar energy applications.

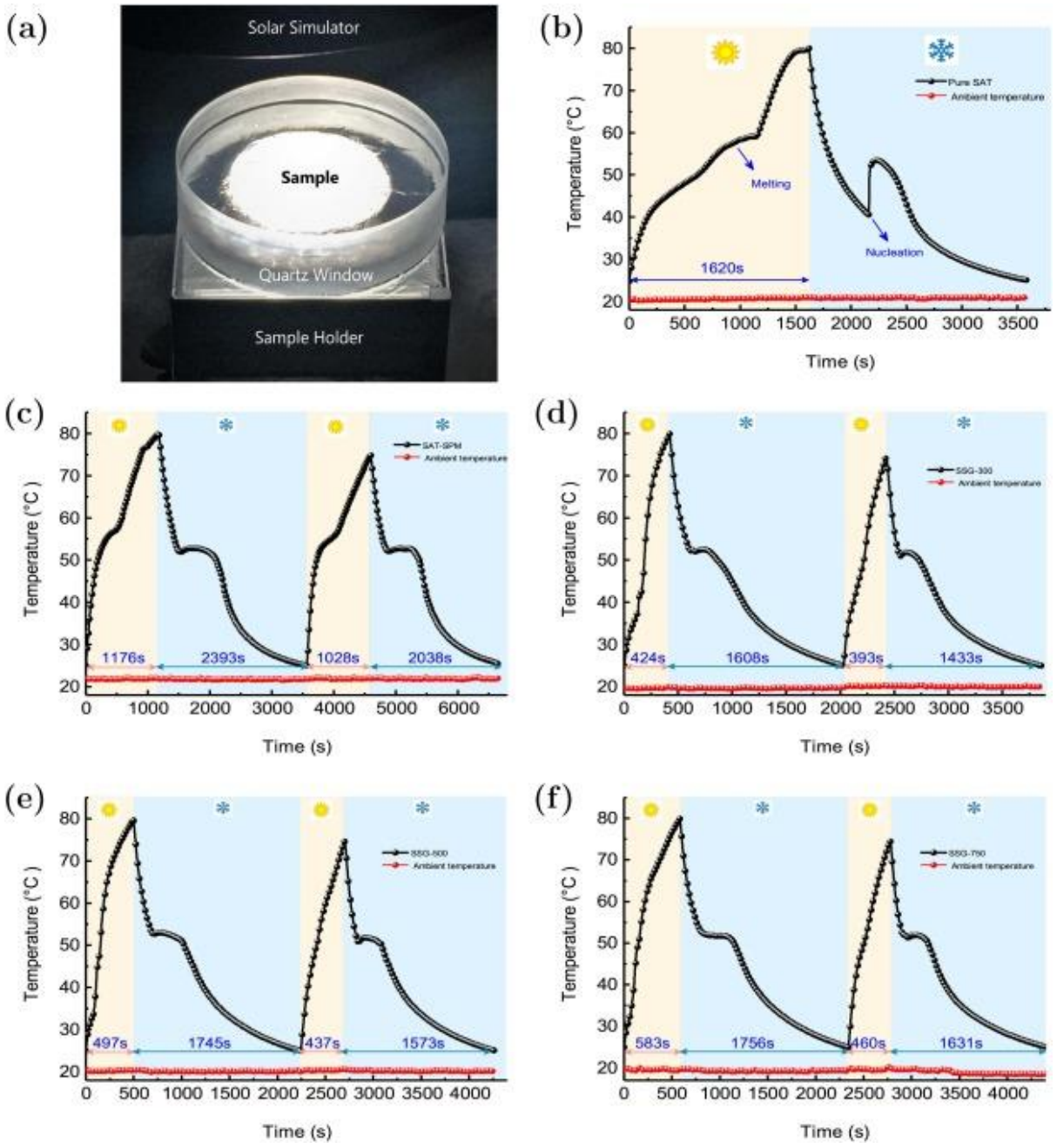

Fig. 7. (a) Photo-thermal setup and solar absorption performance of (b) Pure SAT; (c) SAT-SPM; (d) SSG300; (e) SSG500; (f) SSG500.

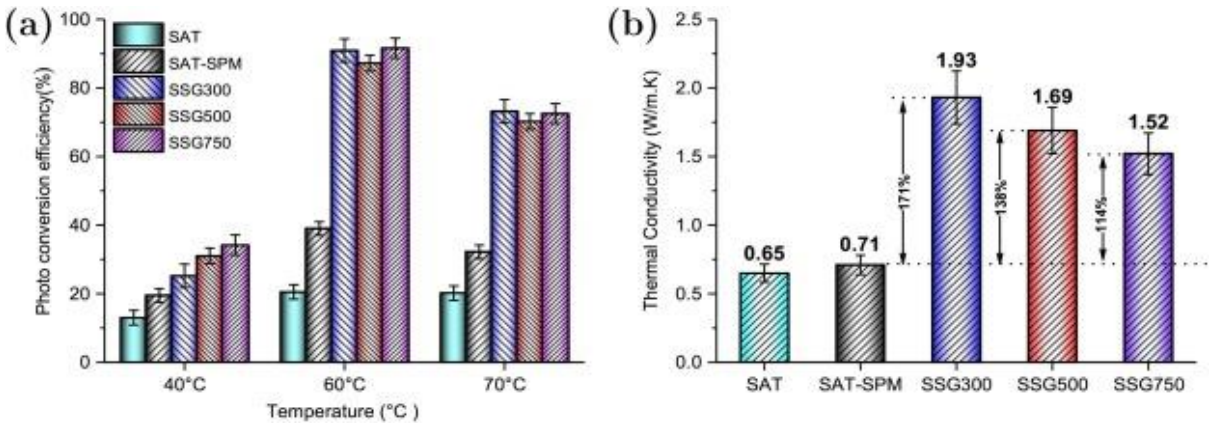

Fig. 8. (a) Photo-thermal efficiency and (b) Thermal conductivity at 30 °C of pure SAT, SAT-SPM and shape stabilized SSG composites.

2.5.9. Thermal conductivity and reliability of SSPCMs

Precise information of a material's thermal conductivity is crucial in heat transfer applications as well as composite PCMs. Importantly, thermal conductivity directly reflects charging and discharging rates of SSPCMs by altering the heat transfer from the heat source to the SSPCM and from the SSPCM to its nearby surroundings. Fig. 8 (b) presents the thermal conductivity values for SAT, SAT-SPM and SSG composite PCMs at 30 °C. The pure SAT and SAT-SPM exhibit low thermal conductivity values of 0.65 and 0.71 W/m.K, respectively. The addition of Hp-GNPs had a significant effect on the thermal conductivity of SSPCMs by enhancing the conductivity up to 2.71, 2.38 and 2.14 times higher than that of the SAT-SPM for SSG300, SSG500 and SSG750,respectively. Undeniably, the high intrinsic thermal conductivity of GNPs can significantly enhance the thermal conductivity of SSPCMs by offering an interconnected graphene nanosheets heat transfer network within the salt structure. The SSG300 composite PCM offered the highest thermal conductivity which can be attributed to higher GNPs loadings or having a larger lateral size and thickness that reduces the phonon scattering at the matrix-bonded interface and results in an effective improvement in the thermal conductivity and heat dissipation ability of the composite. The assessment of physical and chemical stability is very important when considering the prepared SSPCMs for practical applications.

Chapter 3. Simulation of solar collector with phase change materials

A typical solar domestic water heating system suffers from low energy efficiency due to multiple heat transfer process among components, i.e., the solar thermal collector and the thermal energy storage. In this work, a compact design of storage-integrated solar thermal collector and its compatible PCM storage material were explored. The salt hydrate based composite PCM, the SAT was used to create a SSPCMs for a feasible PCM by its low leakage and high thermal conductivity.

3.1. Collector design

In this section, a actual size of solar thermal collector design will be presented in which PCM (i.e., SSE) is used as the absorber and the heat storage medium within the collector. The cylindrical evacuated tube and the double spiral coils heat exchanger are chosen to assemble this collector. The gap between the tube and the heat exchanger is filled with PCM. The water is flowing inside the heat exchanger as heat transfer fluid to realize thermal energy charging and discharging. The collector design process is carried out by geometrical parameters analysis on the double spiral heat exchanger patterns considering both charging and discharging scenarios.

3.2. Collector geometry

Fig. 9 illustrates the geometric characteristic of the solar thermal collector equipped with the double spiral coils heat exchanger. Each coil is characterized by its radius (i.e., R for outside coils, r for inside coils), the pitch as the distance of each turn (i.e., D for outside coils, d for inside coils), and the number of coil turns (i.e., N for outside coils, n for inside coils). By multiplying R and N (or r and n), the obtained values represent the scale of pipes' length. This value is useful for comparing the residence time of the water when it is flowing through the outer or inner coils. On the other hand, the pitch distance influences the water residence time when it is passing the front or bottom area of the tube. The area where has a smaller pitch means a higher density of pipes there, thus the water will have a longer time to exchange the heat with the PCM. These two values describe the outline of the heat exchanger pipes' pattern in radial and longitudinal directions, and they could influence the heat transfer rate and phase change of PCM around the pipes. Table 2 lists all the geometric parameters of each case.

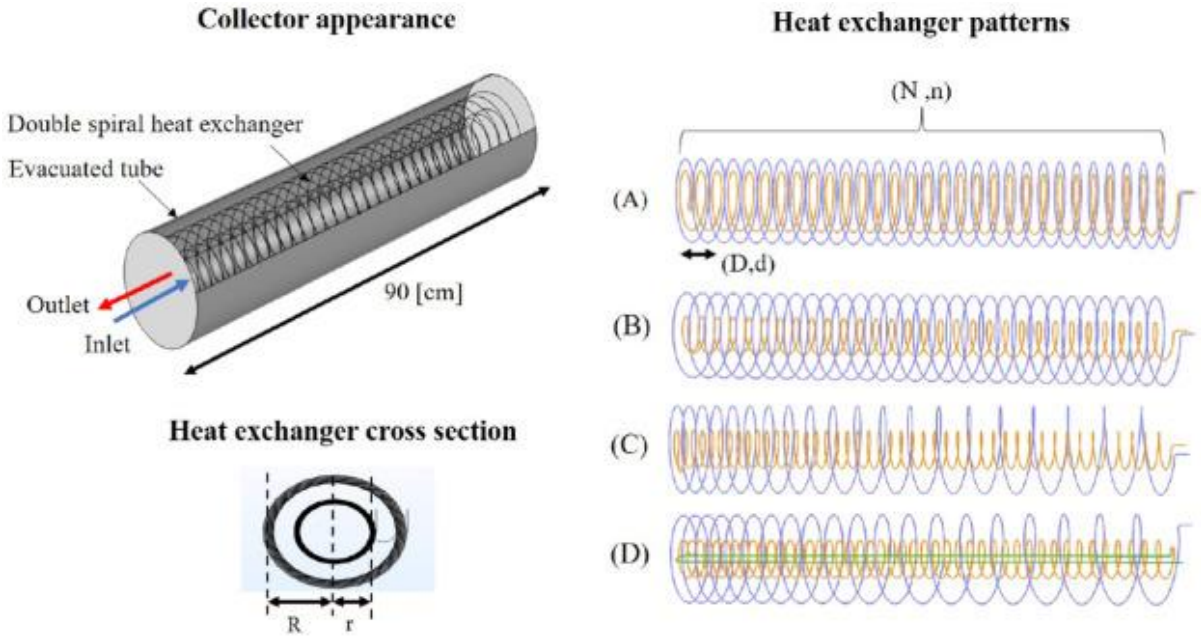

Fig. 9. (a) Schematic diagram of storage-integrated solar thermal collector which are composed of evacuated tube and heat exchanger. (b) Four design cases on different patterns of heat exchanger. Blue line represents the outside coils, orange line is the inside coils, and green line is the central U-pipe.

Table 2. Geometric specification of double spiral coils pipes' pattern, Case (A)-Case (D). In Case (D) an extra set of U-shape pipe is added to the center of the tube.

	Outside coils		**Inside coils**		**Pipes**
Cases	**R x N [cm]**	**Pitch [cm]**	**r x n [cm]**	**Pitch [cm]**	**L_{pipe}[m]**
(A)	210	2.8	150	2.8	22.8
(B)	210	2.8	90	2.8	19.1
(C)	140	2–6.5	135	1.5–2.3	17.5
(D)	140	2–6.5	135	1.5–2.3	19.3

3.3. Discharging and charging scenarios

Separate scenarios are considered for discharging and charging as shown in Fig. 10.

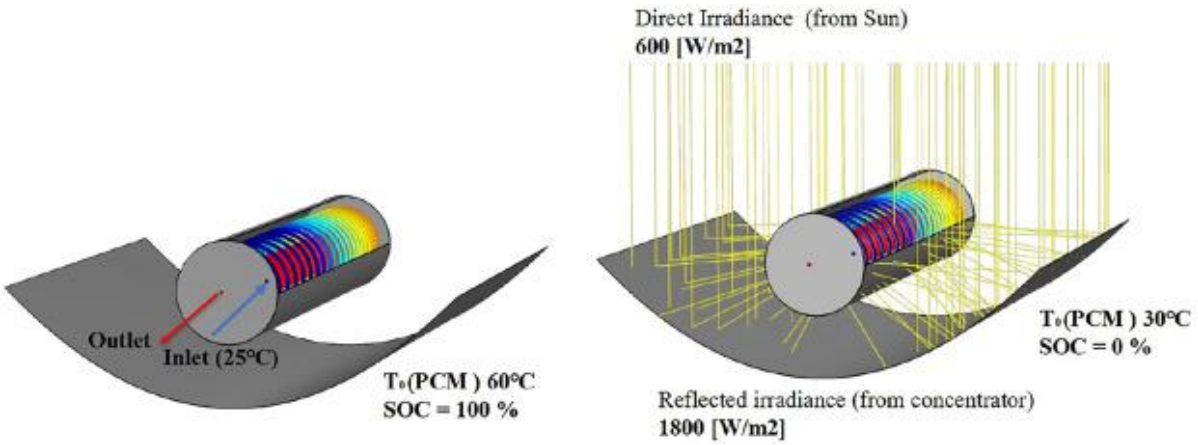

Fig. 10. Diagram of usage scenario testing, discharging (Left) and charging (Right).

3.4. Discharging scenario

The model setup of discharging scenario is shown in Table 3. The cold water enters the collector with constant temperature 25 °C, extracts heat from PCM, and then leaves with a higher temperature. The initial status of PCM is assumed fully charged with an initial temperature T_{PCM} = 60 °C. This scenario is designed mainly to see how much the water's temperature increases after leaving the tube, and also to evaluate the hot water supplying ability by looking at the duration of outlet temperature that remains above 55 °C for fitting the domestic hot water demand (T_{out} > 55 °C).

Table 3. Boundary conditions for scenarios of discharging and charging.

Boundary condition	**Discharging**	**Charging**	
$T_{PCM}(t = 0)$	60	30	◦C
T_{inlet}	25	25	◦C
Mass flow rate	$2e^{-3}$	$4e^{-4}$	kg/s
P_{outlet}	1	1	bar
Top (Bottom) Solar flux	*	600 (1800)	W/m^2

3.5. Charging scenario

In the charging scenario, an active charging rate enhancement method is introduced. During the charging process, water is continuously circulating inside the evacuated tube as a closed system. The role of the circulating water is to actively distribute the irradiated heat that is

absorbed by the PCM near the outer place of tube toward the centre of collector. This increases the charging rate of PCM close to the centre of the tube while preventing a high temperature at the surface of PCM. The irradiance was continually applied to the outer surface of the tube when the water is circulating. The value of irradiance on upward surface of the tube is 600 W/m^2 based on the average irradiation in the Netherlands [33]. As shown in Fig. 6, the downward surface receives a higher irradiation than the upward surface. It is due to the assumption of a concentrator placing underneath the tube to collector the irradiation from top and then reflect toward the downward surface with intensive irradiation. The others boundary condition is shown in Table 3. The simulation results of circulation were compared with the scenario of still water.

3.6. Design indicators for discharging scenario

To compare the performance of each design, indicators were developed for both discharging and charging scenarios. The maximum theoretical discharging time ($t_{max,\ discharge}$) was calculated for the discharging scenario. It indicates the maximum time that collector can apply hot water above 55 °C. This maximum value is derived based on the assumption of no heat loss, the total usage of stored heat in PCM for water heating, and infinite fast heat transfer rate withing the PCM and between the PCM and the water. Using heat balance, we can find the maximum time. In this case, the total amount of PCM is 25.2 kg, the initial temperature of PCM is assumed to be 60 °C (T_0) uniformly, the PCM melting temperature is 57 °C (T_{melt}). The cold water is mean to heat up from 25 °C (T_{in}) to 55 °C (T_{out}), the mass flow rate of 0.002 kg/s. Then $t_{max,\ discharge}$ is calculated as 22,529 s.

3.7. Discharging scenario

Fig. 11 (Top) shows the water outlet temperature (T_{out}), and the PCM's state of charge (Bottom) over time. The initial temperature of PCM is set 60 °C and inlet water temperature is 25 °C. The entering cold water continually extracts the heat from the PCM. The PCMs melting status, referred as state of charge (SOC) value drops while the PCM is being discharged. Then T_{out} decreases over time along with the PCM got discharged.

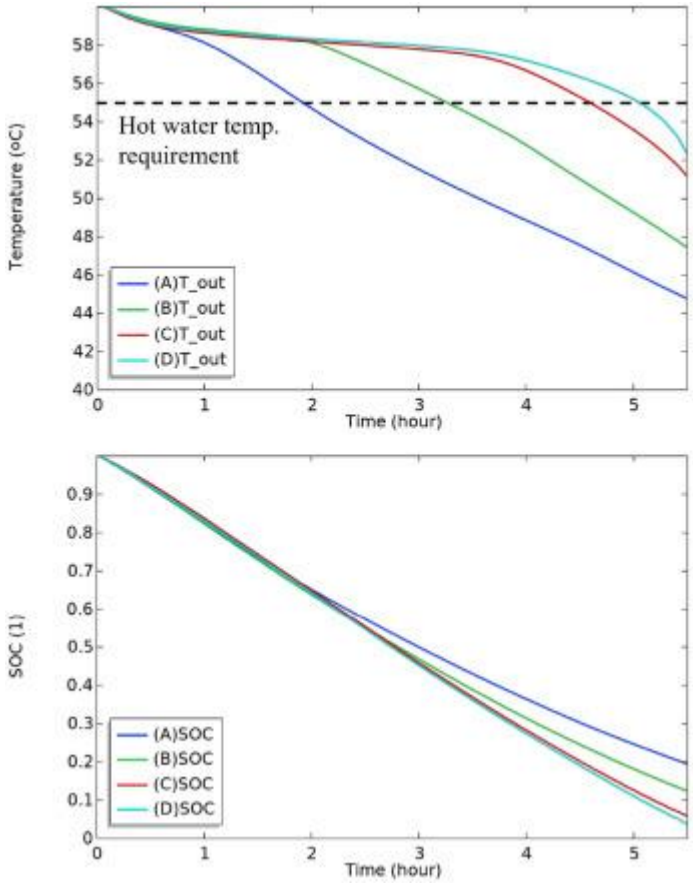

Fig. 11. Outlet water temperature (Top) and PCM's SOC (Bottom) over time during discharging period on four heat exchanger patterns. Dotted line represents the required temperature for domestic hot water.

There is a plateau around 58 °C in every case. It represents the duration that the PCM transforms from liquid to solid. Once the latent heat capacity around the pipes is used up, the PCM temperature will start decreasing to below 58 °C quickly, resulting in a sudden decrease on T_{out}. However, from the simulation results Figs. 11 and 12 could see that the overall PCM discharges unevenly. There are still many PCM left undischarged (SOC > 0) when T_{out} drops below 55 °C. Like the Case (A), the PCM still has 65% in liquid phase as seen in Fig. 7 (Bottom). It reflects a fact that the water contacts with a locally fast-discharged and low-temperature PCM when it leaves the tube. The PCM discharging rate near the outlet area is faster than other places. It results in a low PCM utilization, making a low achievement compared to the maximum theoretical discharging time. In the following discussion, at each case the duration of keeping T_{out} larger or equal to 55 °C is called effective discharging time ($t_{eff,\ discharge}$). The optimal collector design for discharging scenario makes the $t_{eff,\ discharge}$ as close as possible to the maximum theoretical discharging time ($t_{max,\ discharge}$).

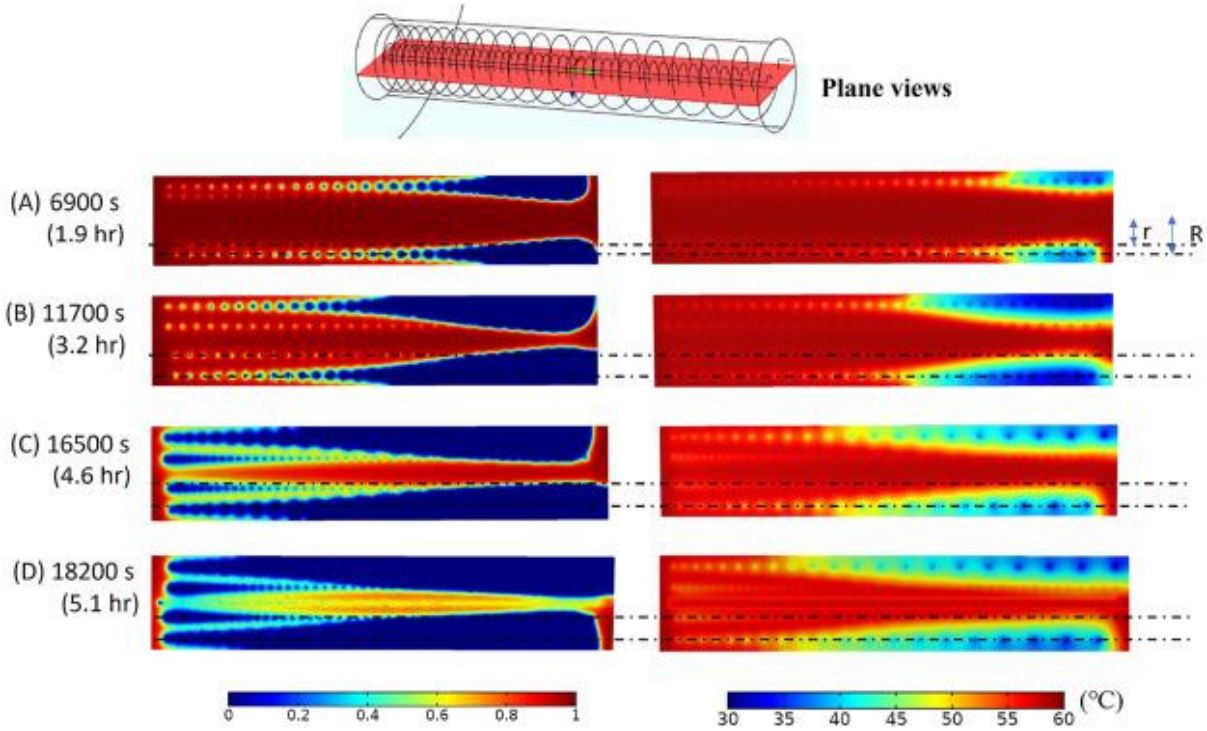

Fig. 12. PCM SOC (Left), PCM temperature (Right) at the end of effective discharging time for each case during the discharging period. Dotted lines are the location of outside and inside coil pipes.

Comparing Case (A) with Case (B), they share mostly the same geometry but only the radius of inside coils in Case (B) is reduced from 5 cm to 3 cm. The total pipe length of Case (B) decreases by 16% compared to Case (A). Logically a shorter pipe will decrease the residence time of the water for the heat exchanging. However, Case (B) brings an advantage of 1.7 times longer of $t_{eff,\ discharge}$ than Case (A). PCM's utilization increases up to 58% (In Case (A) is 35%). The reasons beyond this improvement in Case (B) could be realized by the long-lasting heat extraction driving force throughout the water's flowing path inside the heat exchanger. The heat extraction driving force is proportional to the temperature difference between PCM and the flowing water. A large driving force can promise a high discharging rate. However, a locally extreme large driving force will lead to low uniformity of PCM temperature. Fig. 8 presents SOC (Left) and temperature distribution (Right) of five cases at the moment of $t_{eff,\ discharge}$. When the latent energy at the local PCM is used up, the local temperature will start dropping rapidly into the sensible energy regime and form a cold zone as seen the dark blue area in Fig. 8. The heat extraction driving force near the inlet of the outside coils remains huge due to the continually incoming cold water, causing the PCM there to rapidly accumulate the cold zone. Whenever the cold zone penetrates the outlet area, the ready-to-leave water will experience a cold surrounding. Since the PCM temperature inside the cold zone is lower than melting

temperature which is 57 °C, the T_{out} will expect to drop below than the desired hot water temperature which is 55 °C.

To increase PCM utilization and extend the effective discharging time ($t_{eff,\ discharge}$), the issue of fast cold zone accumulation needs to be solved. From Fig. 8 it could be seen that in Case (A) the unbalanced heat driving force exists in two directions along the evacuated tube, the longitudinal and radial directions. Inside coil pipes in Case (A) are very close to the outside coils. This closeness enhances the discharging rate around the coils. However, the PCM located away from the coils are suffered from low heat exchange rate, resulting in many of PCM are still undischarged when the temperature of leaving water drop below than 55 °C. It is the cause of radial unbalance.

In Case (B), the inside coil is moved away from the cold zone by using a smaller radius for inside coil. The discharging at inside and outside coils are decoupled. It takes the advantage of having a longer duration on utilizing the PCM energy before the cold zone starts influencing the leaving water. The heat driving force is more uniform along the radial direction than Case (A). The inside coil could contribute more on the PCM utilization; thus Case (B) has a longer duration of $t_{eff,\ discharge}$.

Case (C) improves the longitudinal unbalance by applying a variable pitch distance concept as described in Table 2. In Case (C), it applies a smaller pitch distance D1 and d1 at the bottom part of the tube for more discharging. The flowing water at the smaller pitch area could stay for a longer time to have more heat exchange, thus compensating for the issue of a lower driving force at the location far from the inlet area. The variable pitch effect is significant. The $t_{eff,\ discharge}$ in Case (C) achieves 16,510 s, the PCM utilization is as high as 81%. It is worth mentioning that the total pipes length in Case (C) is decreased by 15% compared to Case (A), while $t_{eff,\ discharge}$ increases 2.6 times.

In Case (D), a further solution is brought out. An extra U-shape pipe is added to the centre of the evacuated tube, connected right after the end of the inside coil pipes as seen in Fig. 5. This leads to move the position of the water outlet further away from the cold zone (compared to Case (C)) to avoid the radial cold zone. This approach also utilizes the PCM more at the centreline. In Fig. 8 the SOC and PCM temperature distribution are more uniform in Case (D). The PCM utilization in the central area is improved significantly. The total pipe length in Case (D) is similar to Case (B), while the $t_{eff,\ discharge}$ is doubled in Case (D) compared to Case

(B). Its PCM utilization reaches 90%. These results reflect the importance of PCM utilization near the inside and central area where usually having a lower heat exchange driving force.

Chapter 4. Construction and test of solar collector

In this section, the construction process and the configurations of different tested solar thermal collectors have been explained. Moreover, the implementation of the experiments and the related testing conditions have been clarified.

4.1. Direct-absorption parabolic trough solar collector

The constructed SSPCM-PTSC contains a frame, reflector frame, a double-glazed tube, a ball valve, a parabolic concentrator, and a U-pipe heat exchanger. The aluminium profiles with 40 mm × 1000 mm dimensions were used for the frame of the solar collector and a flexible mirror-like stainless steel with 1000 mm × 1000 mm × 0.8 mm size was utilized as the parabolic reflector. In order to design the frame of the parabolic reflector, the related equation of the parabola has been derived by Parabola Calculator 2.0 software. Then, the parabola has been sketched on the piece of wood with 200 mm depth and 1000 mm diameter using 100 points to obtain a precise parabolic frame for the efficient light concentration purposes of the reflector. Also, of the solar system. Fig. 13 (a) indicates the sketched parabola on a millimetre-graded piece of wood and Fig. 13 (b) shows the cut parabola on the wood to act as the frame of the reflector. In addition, Fig. 13 (c) illustrates the whole frame of the proposed PCM-PTSC with the parabolic frame installed and Fig. 13 (d) demonstrates testing the concentration of light on the focal line of the proposed parabolic concentrator.

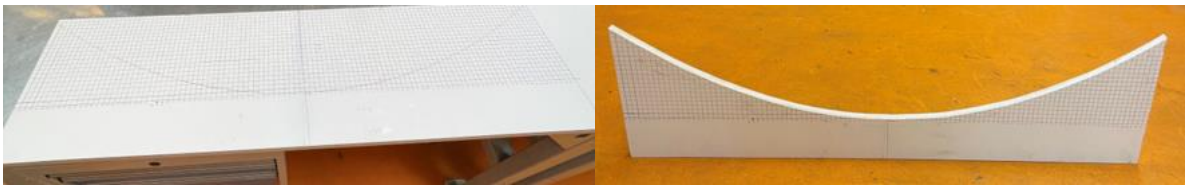

(a) (b)

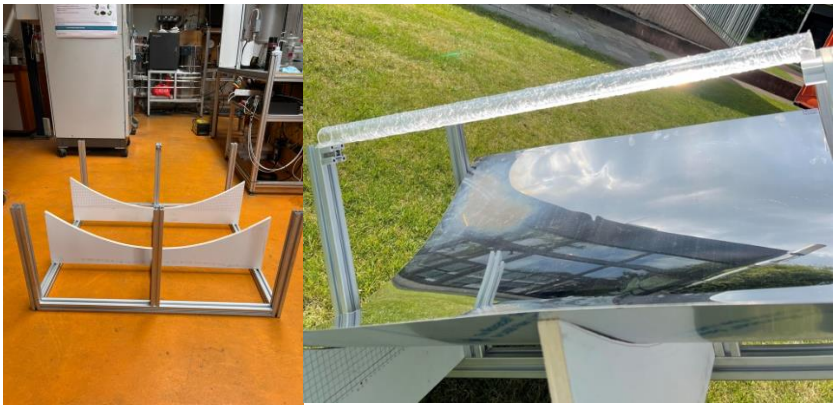

(c) (d)

Fig. 13. (a) The sketched parabola on wood, b) the cut parabola to act as the frame of the reflector, c) the complete frame of the PCM-PTSC including the parabolic reflector frame, d) checking the light concentration performance of the designed and constructed PTSC.

Also, two acrylic acid tubes with 50 mm and 70 mm diameters and 300 mm length were considered to construct the double-glazed tube so that the inner tube was filled with the SSPCM. Also, for reducing the convective heat transfer losses, the air and argon gas have been tested to fill between the tubes and their effects on the performance of the solar collector have been shown. Moreover, a U-pipe made of stainless steel with 4 mm and 6 mm inner and outer diameters and 800 mm length was employed for the water passage for the heat extraction process. Furthermore, a tiny hole and a ball valve was considered at the back of the tube for flushing and filling it with argon and a thermal bath was used for the water flow through the U-pipe heat exchanger. Fig. 14 (a) presents the constructed double-glazed tube along with the U-pipe heat exchanger, and the ball valve at the back. The initial temperature of the bath was set at 20 ^{o}C and the flow rate of water was adjusted using a 3-way valve by measuring the time of filling a certain volume of a graded container as indicated in Fig. 14 (b) and (c).

(a)

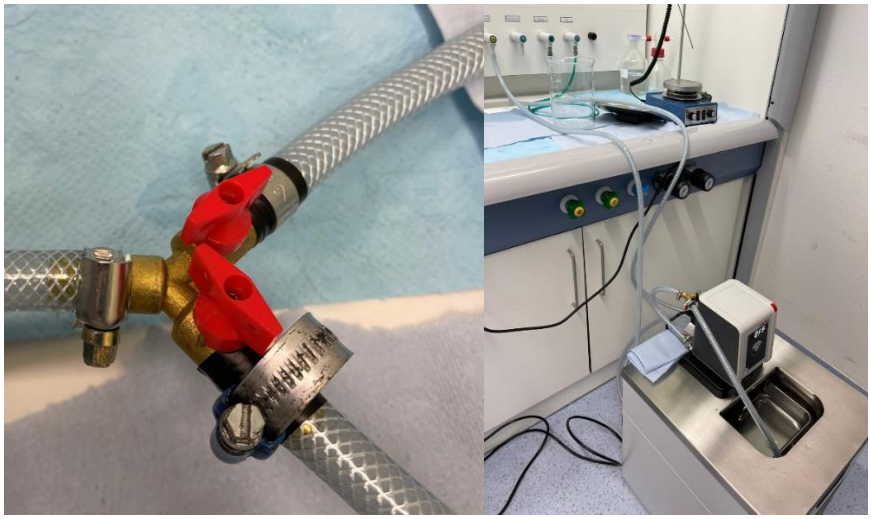

(b) (c)

Fig. 14. (a) The double-glazed tube including the U-pipe heat exchanger and the backside ball valve, b) the employed 3-way valve to adjust the mass flow rate, c) water flow regulation process utilizing a thermal bath, 3-way valve, and a graded container.

4.1.1. Implementation of experiments for the PTC

First, the PTC was tested outdoor with the real sun in a clear sky with different configurations of the U-pipe heat exchanger. Six K-type thermocouples were adopted to measure the temperatures of top, middle, bottom parts of PCM, inlet-outlet of water, and ambient temperatures using an NI data acquisition system. A thermal bath was utilized for the water flow during discharging process and the flow rate of 15 LPH was chosen for the discharging process. Moreover, the solar radiation intensity was measured by a calibrated PV cell with the accuracy measurement of 5-10 W/m^2 and the concentrator was designed to track the sunlight throughout the experiments. Fig. 15 shows the experimental setup of the constructed PTC with the employed SSPCM.

Fig. 15. Experimental setup of the PTC in outdoor experiments.

4.1.2. Results

Fig. 16 shows the temperature variations of the PCM inside the receiver considering horizontal and tilted positions of the heat exchanger. As it can be noticed, when the heat exchanger is horizontal, the top part of the PCM becomes overheated that is not recommended for the PCM. However, if the U-pipe is placed in a tilted way, it cannot only produce heat, also it avoids overheating the PCM. Nonetheless, it was witnessed that the bottom part of PCM reaches above 90 ^{o}C that is not good for the material; hence, it can be concluded that this PTC with this concentration ratio is not suitable for domestic hot water production and non-concentrating solar collector was preferred.

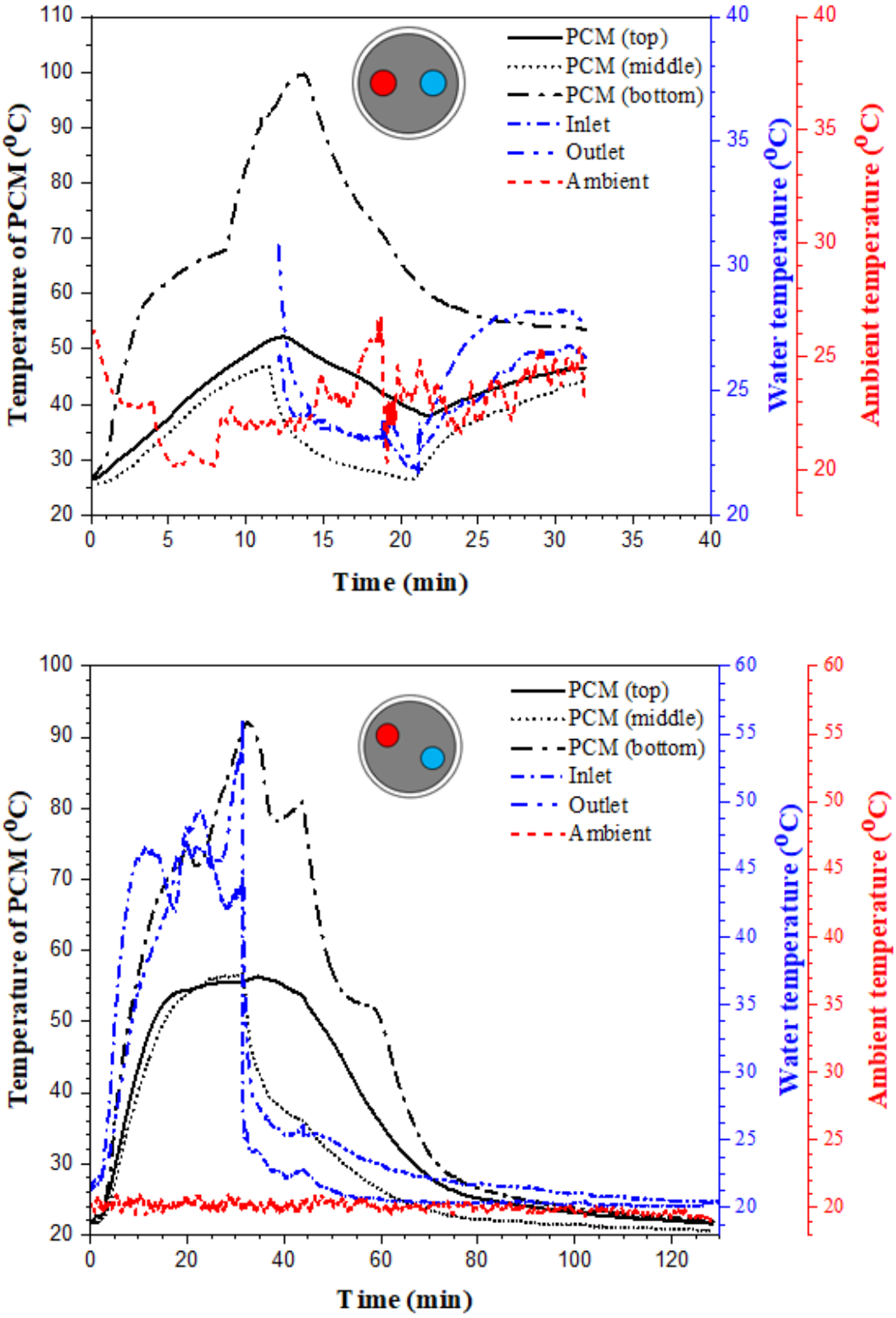

Fig. 16. Temperature variations of the PCM and water for outdoor experiment with the PTC.

4.2. Implementation of the experiment for cylindrical solar collector

After realizing that the PTC is not suitable, the lab experiments were done at two mass flow rates of 15 and 45 litre per hour (LPH) under the radiation intensity of 1.6 kW/m^2 considering horizontal and vertical configurations of the U-pipe (see Fig. 17). Six K-type thermocouples were adopted to measure the temperatures of top, middle, bottom parts of PCM, inlet-outlet of water, and surroundings temperatures using an NI data acquisition system. A thermal bath was utilized for the water flow during discharging process and the flow rate of 15 LPH was chosen for the discharging process.

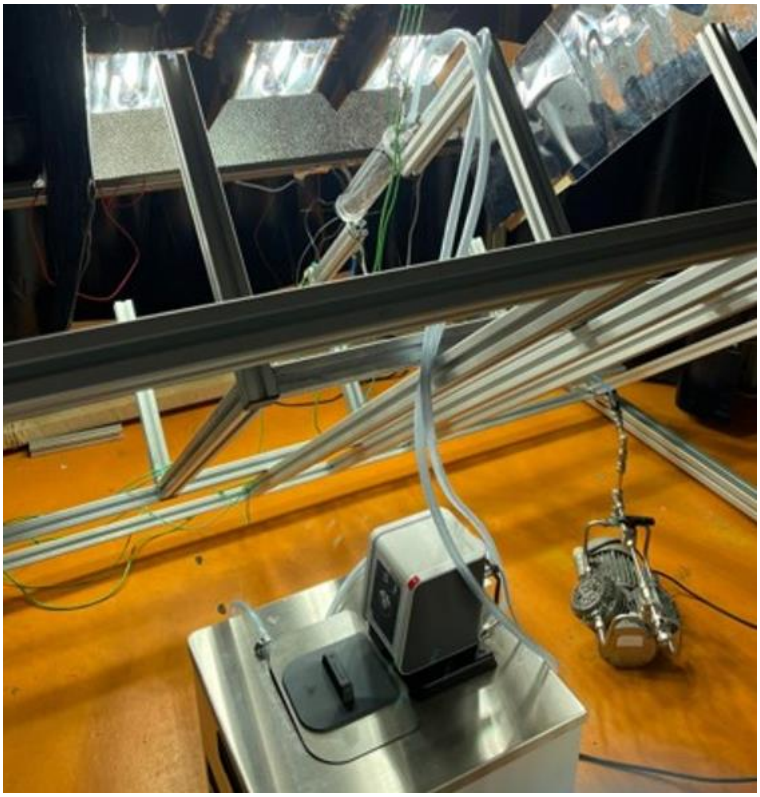

Fig. 17. Experimental setup of the cylindrical solar collector in laboratory experiments.

4.2.1. Results

Fig. 18 indicates the temperature variations of PCM and inlet-outlet water flow for horizontal and vertical positions of the U-pipe heat exchanger through the lab-scale experiments. As it is indicated, the ambient temperature varies within 19 to 22 ^{o}C and all parts of the SSPCM are experiencing similar temperature increase rate due to the PCM high thermal conductivity. Moreover, the PCM charging process has taken around 2 hours that is normal for the solar thermal collector's performance and the average discharging time is 45 minutes that regarding the 300 gr PCM inside the tube, it is acceptable value for the heat storage.

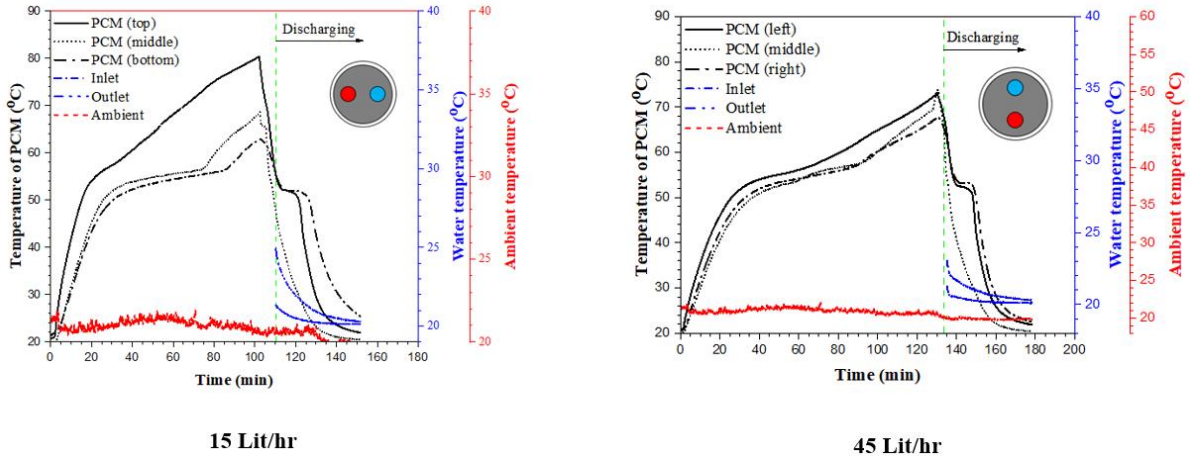

Fig. 18. Temperature variations of the PCM and water for indoor experiment with the cylindrical solar collector.

5. Direction of future work

In the current design, the utilized PTC with the concentration ratio of 20 led to overheating the SSPCM and damage to the PMMA receiver. Therefore, different PTC with lower concentration ratio values should be tested to reach a reasonable solar collector for facilitating the PCM charging process.

Moreover, it was concluded that the direct absorption is very efficient during charging process; however, the radiative heat loss is high during discharging process that can be further investigated by selective coatings for the proposed solar receiver-storage system. On the other hand, the salt hydrate PCMs become too stiff after several charging-discharging cycles that might cause some challenges. Thus, the commercial coated evacuated tube with 0.8 mm glass thickness might not withstand the imparted force as a result of the PCM expansion while melting and this needs to be tested in future work.

References:

[1] T. Fleiter, J. Steinbach, M. Ragwitz, J. Dengler, B. Köhler, F. Reitze, et al. Mapping and analyses of the current and future (2020-2030) heating/cooling fuel deployment (fossil/renewables). European Commission, Directorate-General for Energy. (2016).
[2] F. Wang, W. Lin, Z. Ling, X. Fang. A comprehensive review on phase change material emulsions: Fabrication, characteristics, and heat transfer performance. Solar Energy Materials and Solar Cells. 191 (2019) 218-34.
[3] A. Pandey, M. Hossain, V. Tyagi, N. Abd Rahim, A. Jeyraj, L. Selvaraj, et al. Novel approaches and recent developments on potential applications of phase change materials in solar energy. Renewable and Sustainable Energy Reviews. 82 (2018) 281-323.
[4] G. Englmair, C. Moser, H. Schranzhofer, J. Fan, S. Furbo. A solar combi-system utilizing stable supercooling of sodium acetate trihydrate for heat storage: Numerical performance investigation. Applied energy. 242 (2019) 1108-20.
[5] W. Kong, M. Dannemand, J.B. Johansen, J. Fan, J. Dragsted, G. Englmair, et al. Experimental investigations on heat content of supercooled sodium acetate trihydrate by a simple heat loss method. Solar energy. 139 (2016) 249-57.
[6] W. Kong, M. Dannemand, J.B. Berg, J. Fan, G. Englmair, J. Dragsted, et al. Experimental investigations on phase separation for different heights of sodium acetate water mixtures under different conditions. Applied Thermal Engineering. 148 (2019) 796-805.
[7] M. Dannemand, J.B. Johansen, S. Furbo. Solidification behavior and thermal conductivity of bulk sodium acetate trihydrate composites with thickening agents and graphite. Solar Energy Materials and Solar Cells. 145 (2016) 287-95.
[8] F. Qiu, S. Song, D. Li, Y. Liu, Y. Wang, L. Dong. Experimental investigation on improvement of latent heat and thermal conductivity of shape-stable phase-change materials using modified fly ash. Journal of Cleaner Production. 246 (2020) 118952.
[9] Y. Qu, S. Wang, Y. Tian, D. Zhou. Comprehensive evaluation of Paraffin-HDPE shape stabilized PCM with hybrid carbon nano-additives. Applied Thermal Engineering. 163 (2019) 114404.
[10] X. Huang, X. Chen, A. Li, D. Atinafu, H. Gao, W. Dong, et al. Shape-stabilized phase change materials based on porous supports for thermal energy storage applications. Chemical Engineering Journal. 356 (2019) 641-61.
[11] Q. Xiao, J. Fan, Y. Fang, L. Li, T. Xu, W. Yuan. The shape-stabilized light-to-thermal conversion phase change material based on CH3COONa· 3H2O as thermal energy storage media. Applied thermal engineering. 136 (2018) 701-7.
[12] B. Li, X. Zhai. Experimental investigation and theoretical analysis on a mid-temperature solar collector/storage system with composite PCM. Applied Thermal Engineering. 124 (2017) 34-43.
[13] D.N. Nkwetta, F. Haghighat. Thermal energy storage with phase change material—A state-of-the art review. Sustainable cities and society. 10 (2014) 87-100.
[14] Z. Wang, F. Qiu, W. Yang, X. Zhao. Applications of solar water heating system with phase change material. Renewable and Sustainable Energy Reviews. 52 (2015) 645-52.